Automated X-ray computer tomography segmentation method for finite element analysis of non-crimp fabric reinforced composites

N.B. When citing this work, cite the original published paper.

(article starts on next page)

Automated X-ray computer tomography segmentation method for finite element analysis of non-crimp fabric reinforced composites

Robert M. Auenhammer [a,b,*], Lars P. Mikkelsen [b], Leif E. Asp [a], Brina J. Blinzler [a]

[a] Department of Industrial and Materials Science, Chalmers University of Technology, Hörsalsvägen 7A, SE-41296 Göteborg, Sweden
[b] Composite Materials, DTU Wind Energy, Technical University of Denmark, DK-4000 Roskilde, Denmark

ARTICLE INFO

ABSTRACT

In this study a complete procedure is presented of how to generate finite element models based on X-ray computer tomography data on the fibre bundle scale for non-crimp fabric reinforced composites. Non-crimp fabric reinforced composites are nowadays extensively used in the load carrying parts of wind turbine blades. Finite element analysis based on X-ray computer tomographic data will allow faster and cheaper developments of key material parameters. However, automated procedures for computer tomography data transfer into finite elements models are lacking. In the current study, an X-ray computer tomography aided engineering (XAE) process including a fully automated segmentation method and an element-wise material orientation mapping of X-ray computer tomographic data is presented for the first time. The proposed methodology combines recent research progress and improvements in image analysis, and provides a fast, accurate and repeatable data transfer and analysis process with a high degree of automation.

1. Introduction

Fibre-reinforced composites are used in applications where high stiffness and low weight are desired. Their main advantages are good mechanical properties (high stiffness and strength), low density, their ease of manufacturing, resistance against corrosion, design flexibility, high fatigue endurance and the possibility of adapting mechanical properties to the requirements [1]. These are some of the reasons why the growth rate of usage of composites is higher than the growth rate of steel or aluminium the last past decades [1].

1.1. Non-crimp fabric reinforced composites

Non-crimp fabrics are used for fibre reinforced composites which in particular have become more and more popular. They were originally developed for applications in aeronautics consisting of 4000–24000 carbon fibres per yarn [2]. The non-crimp fabric composites considered for wind turbines consist of bundles of fibres all oriented in one direction and stitching yarns to ease manufacturing and handling. Because of their good cost to stiffness relation they are nowadays often used for the load carrying parts in wind turbine blades where material cost reduction is essential for further growth of the wind energy industry [3]. The trend in the wind turbine industry is moving towards lar-

ger blades since the generated power is proportional to the blade length squared [4]. Due to the high aerodynamic and gravitational forces accompanying these longer blades, a higher stiffness is required. This is mainly achieved with non-crimp fabric reinforced composites, which offer a good performance for the dominating bending loads [5]. In order to improve the key performance of non-crimp fabric composites it is important to understand how the stiffness of the composite depends on the structure at different scales. The structure of the fibres themselves on one scale, the fibre bundles as well as the bundles-matrix interface and the structure on other scales are of interest. Damage can occur on all these scales during cyclic loading. The generated fatigue damage immediately results in reduced stiffness which can be tracked with damage sensing methods in blades e.g. modal analysis [6]. It is vital to understand how these damage mechanisms contribute to this reduced stiffness in order to estimate the fatigue life of the structure.

1.2. X-ray computer tomography

X-ray computer tomography was originally developed in the 1960s and its first application was in the medical field, where it is important to scan as many patients as fast as possible by keeping the radiation dose on them as small as possible. Later in the 1970s and 80s it was

also used in non-medical research and industry [7]. In contrast to common radiography, where the entire information of the transmitted object is projected to a detector in one shot, the sample is turned around itself and exposed to the X-ray beam from different angles in order to get many 2D projections (Note: It is also possible to rotate the X-ray source and detector around the sample). By this procedure 3D information about the size and position of an object inside the scanned sample is added. The outcome of the acquisition is a collection of line integrals. The line integrals need to be reconstructed to obtain an image of the scanned object from a finite number of samples [8]. This inverse problem can be approached with two methods, variants of the so called filtered back-projection and iterative algebraic methods [9]. Modern reconstruction algorithms allow for suppression of artefacts [10]. Examples of such artefacts are; incorrect vertical elongation and disappearance of horizontal structures due to for example limited tilting angles for electron tomography [11] or quasi real time reconstruction used for airport security scanners [12].

X-ray computer tomography has proven its ability to characterise important material parameters, not only stiffness, strength and fatigue behaviour for polymer matrix composites but also for materials like concrete or metals [13–15]. The attenuation contrast offered is not as distinct as for glass fibres and matrix, but it can be enhanced by using phase contrast. The need in industry and research for X-ray computer tomography has led to lower prices and improvements in the image acquisition as well as in the following processes (reconstruction and segmentation) due to active research in recent decades.

For investigations of fatigue performance it has been a well-documented approach to run a fatigue test and capture the crack propagation by X-ray computer tomography scans [5,13–16]. The crack growth can be followed and visualised in 3D and the sample does not have to be destroyed in order to obtain an image of the situation inside the structure. Beside the non-destructive character X-ray computer tomography offers high resolution [17–19], even though it cannot compete in terms of maximum resolution with scanning electron microscopes. However, for composites often the fibre scale of a few microns is of interest, which is a standard resolution for tomographic scanners. There are two options to correlate X-ray computer tomography data to mechanical testing. One is the so called *in situ* method, where the sample is scanned during the load application. Wang et al. [20] have reported an *in situ* four-point-bending test. The challenge for this approach lays in the often limited space available for mechanical testing inside a scanner. Moreover, the time a scan takes can be much longer than the time period, that is of interest, for example an abrupt material failure. More common is the *ex-situ* method where the sample is under no time dependent loading or no loading at all. Wilhelmsson et al. [21] carried out a compression test on a carbon fibre non-crimp fabric composite specimen and scanned the sample before and after failure. Jespersen et al. [5] and Zangenberg et al. [22] also ran *ex-situ* tests on glass fibre non-crimp fabric composites, similar to those addressed in the current study. One conclusion of their studies on non-crimp fabric composites under tension fatigue load was a new fatigue scheme that suggests single fibre failures occur already at the first few cycles. The reason for those early fibre cracks were deduced to be stress concentrations that have their origin in the composite's fibre architecture [5]. One goal of this current study is to create a finite element model based on X-ray computer tomography data that is able to detect these stress concentrations.

1.3. Segmentation

Segmentation is often the bottle neck in an X-ray computer tomography aided engineering (XAE) process for fibre reinforced composites. Emerson et al. [18] laid the foundation for fibre tracking for X-ray computer tomography scans and scanning electron microscopy images in Matlab®. A different technology was recently published by Kim et al. [23] where they apply X-ray scattering tensor tomography with circular gratings at continuous carbon fibres embedded in a polymethyl methacrylate matrix. X-ray scattering tensor tomography enables fast detection of fibre orientations in a large field of view compared to classical X-ray computer tomography. Beside continuous fibre composites, short fibre reinforced plastics are also of interest for industry [24], especially in the automotive field. Short fibre composites are used for interior as well as exterior parts with certain stiffness and crash requirements. Usually the fibres are orientated in the flow direction of the injection moulding process which leads to different orientations along the flow or random orientations at the meeting point of flow fronts [25]. Kagias et al. [26] used diffractive small angle X-ray scattering imaging to analyse the fibre orientation of moulded short fibre composites. Tucker together with Advani [27] and Bay [28] used the structure tensor method to predict the fibre orientation for moulding processes for short fibre composites. This method can be also used to analyse image data by determining the eigenvalues of the material orientation. The smallest eigenvalue indicates the fibre direction. Karamov et al. [29] compared the performance of the structure tensor analysis with high-fidelity fibre identification methods (ellipsometry and 3D fibre identification with the commercial software package Avizo™ from Thermo Fisher Scientific [30]) for continuous glass fibre composites. In order to evaluate the performance of the methodologies the sample was scanned with resolutions of $1.4, 3.2, 8$ and $16 \ \mu m$ for a fibre diameter of $17 \ \mu m$. Avizo™ fibre tracking and ellipsometry were only used for the two highest resolutions, in contrast to the structure tensor analysis which was applied to all resolutions. The authors conclude that all methods deliver accurate results, although the 3D fibre identification from Avizo™ is computationally heavy, which was regarded as major drawback. They also state that the Avizo™ tool only works for high image resolutions which allow for identification of the individual fibres.

Huang et al. [31] published an extensive study with their manual segmentation tool on engineering textiles. For their segmentation method they use a software called CompoCT. Despite the described accuracy in the paper, the approach is manual. This creates a labour-intensive process. Furthermore, the accuracy of the analysis results relies on the skills of the operator and number of cross-sections considered. Their study emphasises the achievable accuracy of the method.

1.4. Modelling based on tomography data

There are two ways to create finite element meshes based on tomography data [32]. One is a direct mesh creation from the data, a so-called voxel based approach [33]. This can be fast for simple geometries and 2D applications. Straumit et al. [34] used the structure tensor analysis for their voxel model. With the information of the fibre orientation a finite element model can be created directly from the image data. The other option to transfer tomography data to finite element models is geometry based. Therefore a surface geometry of the scanned object is created and afterwards a finite element mesh is applied [33].

One of the first studies combining computer tomography with finite element analysis was published in 2008 by Badel et al. [35]. They scanned a woven composite in its undeformed and deformed states at the mesoscopic as well as macroscopic scales and validated their simulation model with the X-ray computer tomography scans. Even though this research field has seen huge improvements and they had to deal with limitations in computational power as well as the capabilities of the tomographic scanners, their study provides groundwork for future research. Naouar et al. [36] conducted a similar study on 3D orthogonal non-crimp woven fibres, yet they included a comprehensive segmentation algorithm.

Iizuka et al. [37] investigated carbon fibres embedded in an epoxy matrix. The finite element model in their paper was created out of X-ray computer tomography data that was used to track the fibre position and waviness. Their segmentation algorithm produced intersect-

ing fibres which were deleted to avoid numerical issues. In the end, forty-four single fibres and the surrounding epoxy matrix were included in the model. Blinzler et al. [38] on the other hand, developed a finite element model considering thousands of fibres based on X-ray computer tomography data. In this case the single fibre could not be meshed and modelled. Consequently, the model considered the bundle level and the connections between the bundles and the matrix. The creation of a multi-scale model that combines the fibre and fibre bundle scales can be challenging. A study on multi-scale modelling of orthogonal woven composites was recently published by Tao et al. [39]. In their model multiple statistical uncertainties are implemented on different length scales. Consideration of probabilistic multi-scale mechanical properties can lead to more realistic simulations and better designs.

Jespersen et al. [40] used a segmentation approach where fibre bundles were segmented manually in different cross-sections. The domains between 2D segmentations were interpolated with the commercial software packages Avizo™ and Geomagic Wrap®. This interpolated data was then applied with a finite element mesh. Three different local coordinate systems were used to reflect different main orientations, but bundle waviness could not be represented.

1.5. Objective

To the authors' knowledge, to this date no study that proposes a highly automated procedure that combines an automated segmentation method of X-ray computer tomography data for a complex composite lay-up with a multi-scale finite element modelling analysis has been published. Previous studies in literature focus on different specific fields, e.g. fibre tracking or bundle segmentation. In the current study, these fragmented approaches are assessed and combined in one complete and highly automated process. The main objective of this paper is to develop a highly automated process to transfer of X-ray computer tomography data into robust and reliable finite element models of mechanically loaded non-crimp fabric reinforced composites. At the heart of such a process are procedures for automated segmentation of the fibre bundles. The quality of the finite element model will be evaluated for its ability to predict Young's moduli of unidirectional non-crimp fabric reinforced composites loaded in tension, and for its ability to identify stress concentrations at the position of backing fibre bundles known to initiate fibre fractures under fatigue loading.

2. XAE – X-ray computer tomography aided engineering

X-ray computer tomography aided engineering (XAE) defines the process of how to transfer X-ray computer tomography data into numerical models. The process is visualised in Fig. 1. The novelty in this proposed procedure is combined in its core process with the image acquisition, automated segmentation, meshing and mapping. The XAE core process is described in detail in Chapter 3. In addition to the core process, the sample preparation, fibre volume fraction determination and a material model definition are essential for the XAE process for fibre reinforced composites. The validation process only consists of mechanical tests in this scheme. Yet other validations are also performed to verify the newly developed method.

2.1. Support process

In the following, the single sequences of the support process are presented and discussed.

2.1.1. Sample preparation
To apply the XAE process non-crimp fabric reinforced composites were produced. The same architecture as used by Jespersen et al. [41] for their fatigue assessment was chosen. The composite consists of four layers of unidirectional bundles (with approximately 4000 fibres each) stacked on each other. The fabrics were infused with an unsaturated polyester matrix by the vacuum assisted resin transfer moulding technique. The matrix was cured at room temperature for 24 h and post-cured for 16 h at 313 K. The unidirectional bundles are supported by rather randomly spaced overlapping off-axis backing bundles oriented at approximately $\pm 80°$. The stacking sequence can be described with $[b/0, b/0]_s$, denoting "b,0" as a layer of backing bundles oriented at $\pm 80°$ followed by a layer unidirectional bundles oriented at $0°$. The architecture can be seen in Figs. 3 and 6.

The laminates were milled into tensile test specimens as described by Jespersen et al. [5]. Tabs were adhered to each side of the grip section at the bottom and top to both prevent the samples from slipping in the clamps of the tensile test machine and avoid crushing of the specimen (Fig. 2).

2.1.2. Fibre volume fraction determination
For assigning material properties in the simulations later on, it is crucial to know an exact value of the local fibre volume fraction. Due to the large stiffness difference between the matrix and glass fibres, significant errors of the fibre volume fraction will result in poor predictions of the finite element model.

$$V_{fbundle} = \frac{W_{FAW} \; n}{\rho} \frac{A_{surf}}{\chi_{bundle}} \tag{1}$$

The average fibre volume fraction is calculated with Eq. (1), where W_{FAW} is the fibre areal weight in the normalised $1\,m \times 1\,m$ area from Table 1, n the number of bundle layers over the thickness, ρ is the density of the glass fibres, χ_{bundle} the volume of all unidirectional bundles, A_{surf} the area of the scanned surface parallel to the main fibre direc-
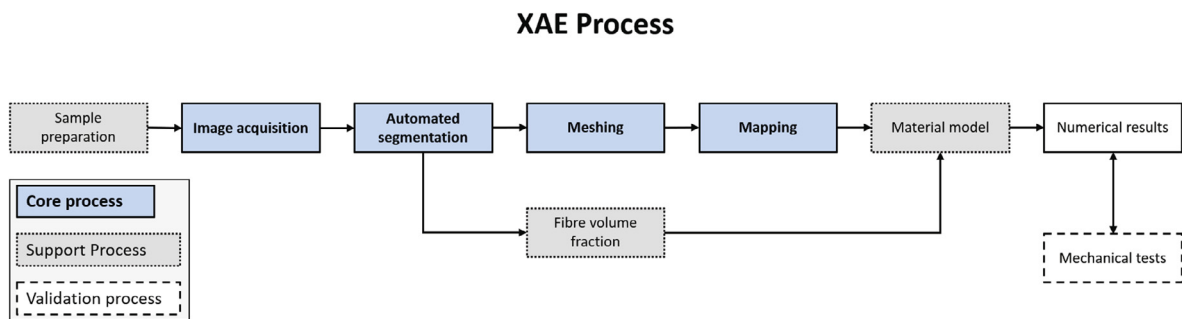
XAE Process

Fig. 1. XAE - X-ray computer tomography aided engineering process with the core elements image acquisition, automated segmentation, meshing and mapping as well as the support process with sample preparation, fibre volume fraction determination and material model definition. The numerical results are validated with mechanical tests.
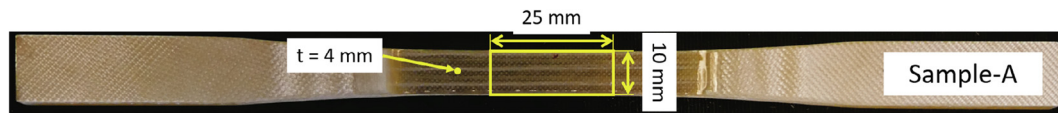
Fig. 2. One out of three produced samples that were tested in the tensile machine. The laminate has a stacking sequence of $[b/0, b/0]_s$ as used in [41]. Details of the manufacturing and geometry of the sample can be found in [5]. The width in the gauge section is approximately 10 mm and the thickness 4 mm. The strain gauge used for the tensile test was applied in the middle of the sample and has a length of 25 mm.

Table 1

Specifications of the used isotropic constituents for the non-crimp fabric reinforced composite.

Category	Unit	Axial fibres	Backing fibres	Matrix
Type	[–]	H+ glass	E-glass	Polyester
Normalised stiffness	[–]	1.0	0.82	0.033
Poisson's ratio	[–]	0.2	0.2	0.35
Density	$[g/cm^3]$	2.6	2.6	1.8
Fibre areal weight	$[g/m^2]$	1322	60	–
Avg. filament dia.	$[\mu m]$	17 and 24	9	–

tion. Note that the value for χ_{bundle} is determined based on the outcome of the segmentation described in the following chapter. The resulting fibre volume fractions are reported in Table 2.

2.1.3. Material model definition

For the subsequent finite element analysis, a decision must be made which material model to choose and which values of the parameters to assign. Since only small deformations will be simulated a linear elastic material model is regarded sufficient. For the matrix surrounding the fibre bundles an isotropic material model is used. The fibre bundles themselves are modelled with an orthotropic material model. Consequently, nine parameters need to be defined. For this purpose the computational homogenisation method applying periodic boundary conditions "Easy PBC" was used [42]. It was chosen for its robustness and high-quality results. Easy PBC is a plug-in for ABAQUS CAE™ which allows to obtain the stiffness parameters as well as Poisson's ratios. This was done for all three analysed specimens (Sample-A, Sample-E and Sample-G), since they have different mean fibre volume fraction inside the fibre bundles. The stiffness values, normalised with the H+ glass fibre stiffness, and the Poisson's ratios are listed in Table 3.

2.2. Validation process

The numerical results were validated with mechanical tests. Scanning electron microscopy images are not necessary for the XAE process, but they were performed to validate the accuracy of the determined fibre volume fraction, see Table 2.

2.2.1. Scanning electron microscopy

The calculated fibre volume fraction inside the bundles depends largely on the outcome of the segmented volume. Since the segmentation method, which will be described in the next chapter, is newly developed the results need to be validated. The images obtained with the X-ray scanning do not allow a fibre volume fraction determination due to their low resolution. Scanning electron microscopy on the other

hand provides high resolution images with a contrast that allows an image-based fibre volume fraction determination. Since the fibres are assumed to be continuous the value is assessed to be representative. However, the obtained value only reflects the fibre matrix ratio in the cross-section that was analysed with the scanning electron microscope.

Scanning electron microscopy comes with the disadvantage that the specimen needs to be destroyed. Thus, this investigation can be only done after mechanical tests and X-ray scans have been performed. The images were taken at DTU (Technical University of Denmark) Roskilde, Denmark with a VEGA3 SBU at a high tension of 20 kV and a backscatter (BSE) detector. Different pixel sizes with 346.02 nm, 349.65 nm and 253.80 nm for sample A, E and G were chosen. The result for Sample-A is depicted in Fig. 3.

From the scanning electron micrographs, the fibre volume fraction inside the fibre bundles was determined by a threshold operation, separating fibre and matrix, and performing a pixel count. The ratio of thresholded fibre pixels and total pixels was calculated for all visible bundles. The mean value of all bundles for each sample is listed in Table 2. The difference between the two fibre volume fraction determination methods is small. Thus, the newly developed segmentation method is found to be accurate for determination of fibre volume fraction for this composite architecture.

2.2.2. Mechanical test

Three displacement controlled tensile tests were carried out at DTU Roskilde, Denmark. Each sample was tested four times to a strain of 0.35% along the main fibre direction. The strain was measured with an extensometer with a gauge length of 25 mm. The test speed was 2 mm/min, hence the tests can be regarded as quasi-static. The stiffness was evaluated between the strains of 0.05% and 0.25%.

The normalised stiffness from the three tests is presented in Table 4. The results were normalised with the single fibre stiffness. The standard deviation of the average stiffness is 0.0078. This low standard deviation cannot explain the difference between the longitudinal stiffness of the samples. Thus, the reason must most likely be found in the

Table 2

Mean fibre volume fractions inside fibre bundles and for the full sample for all three specimen calculated according to Eq. (1), validated with an image analysis of scanning electron micrographs.

Fibre volume fraction	Method	Sample-A	Sample-E	Sample-G
Inside bundles	Calculated Eq. (1)	0.59 ± 0.02	0.61 ± 0.02	0.59 ± 0.02
	Scanning electron microscopy	0.62 ± 0.02	0.61 ± 0.02	0.61 ± 0.02
Composite	Calculated based on Eq. (1)	0.51 ± 0.02	0.53 ± 0.02	0.52 ± 0.02

Table 3

Calculated material properties of the unidirectional fibre bundles by Easy PBC. The stiffness values are normalised with the H+ glass fibre stiffness value.

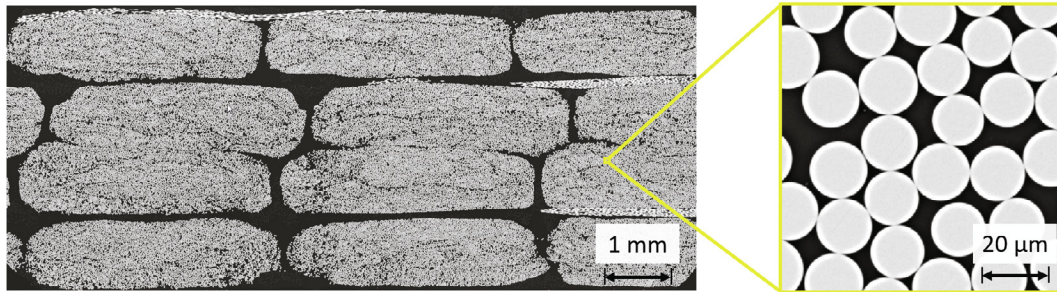|	E_{11} [–]	E_{22} [–]	E_{33} [–]	G_{12} [–]	G_{13} [–]	G_{23} [–]	ν_{12} [–]	ν_{13} [–]	ν_{23} [–]
Sample-A	0.61	0.15	0.15	0.046	0.046	0.032	0.25	0.25	0.27
Sample-E	0.62	0.16	0.16	0.049	0.049	0.034	0.25	0.25	0.25
Sample-G	0.60	0.15	0.15	0.045	0.045	0.032	0.25	0.25	0.27

Fig. 3. Scanning electron micrograph for determining the fibre volume fraction. The images can be downloaded at [43].

Table 4

Experimental tensile stiffness values for Sample-A, Sample-E and Sample-G normalised with the H+ glass fibre stiffness value. The according normalised standard deviation of the mean value is 0.0078.

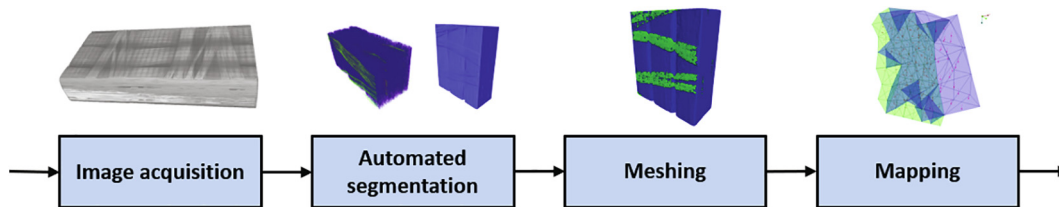|	Sample-A	Sample-E	Sample-G
Normalised stiffness	0.506	0.535	0.519

Fig. 4. Core process of the XAE (X-ray computer tomography aided engineering) process with the key elements Image acquisition, Automated segmentation, (finite element) Meshing and (the element-wise fibre orientation) Mapping.

layup structure of the samples. The developed XAE method is employed to investigate if differences in material architecture can explain the measured differences in stiffness.

3. XAE core process and its application

This chapter presents the core part of the XAE process. Fig. 4 illustrates the proposed method in this study. Central to the proposed procedure is the automated segmentation including a material orientation analysis. Additionally, an element-wise material orientation mapping for the fibre orientations is implemented in the procedure.

3.1. Image acquisition

The X-ray computer tomography scans were performed at DTU Roskilde with a Zeiss Xradia Versa 520 scanner, that has a 2000×2000 pixels detector, depicted in Fig. 5. Two samples were scanned with a so-called binning of 2. This signifies that 2×2 pixels are combined to one single pixel. This lowers the resolution but comes with the advantage of a shorter scanning time and reduced data size. One sam-
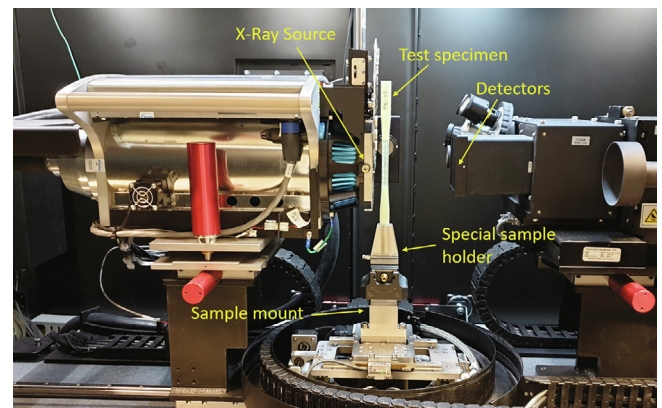

Fig. 5. Zeiss Xradia Versa 520 scanner at DTU Roskilde with the Sample-E. The sample is placed as close as possible to the X-ray source in order to lose as few photons as possible to reduce the exposure time per projection.

Table 5
Scanning parameters at the used Zeiss Xradia Versa 520 scanner at DTU Roskilde. Note that all samples have been stitched together from three single scans.

Sample name	Binning	Exposure time [s]	No. of projections	Accelerating voltage [kV]	Voxel size [μm]	Optical magnification	Scanning time [h]
Sample-A	2	4	3601	50	10.9	0.4×	21
Sample-E	1	16	4501	50	5.47	0.4×	72
Sample-G	2	12	5801	40	10.9	0.4×	66

ple was scanned with a binning of 1 in order to investigate the influence on the segmentation and simulation results. The binning 1 gives half the voxel size but signifies more than three times the scanning time. Further details about the scanning parameters can be found in Table 5. It is not possible to obtain a full scan of the specimens with the desired resolution. However, for all three samples three single scans were performed and the results were stitched together to cover a larger field of view. After removing beam cone effects data with a physical length of approximately 20 mm was obtained. For this study the entire thickness and width of the sample could be scanned. This also avoids dealing with boundary modelling inside the volume. Thus, further investigations are necessary to define the smallest region of interest to still correctly model the material behaviour. After the images have been acquired, they need to be reconstructed. Reconstruction is an essential work step in order to generate images from the acquired computer tomography data. The reconstruction algorithm used in the current study is state of the art. Still the results must be checked for artefacts which may originate from the reconstruction process [44]. The final reconstructed and rendered X-ray computer tomography data image for Sample-G is shown in Fig. 6.

3.2. Automated segmentation

Modern commercial software or freeware offer solutions for segmentation in many different applications, for example medical applications or airport security. Also, Matlab® or Python have special functions to segment reconstructed X-ray computer tomography data. These can be categorised into automatic and interactive approaches. Automatic methods are mostly based on thresholding or watershed codes. Thresholding uses the different grey-scale values of objects in an image to separate them from each other. This technique is widely used and can be regarded as a standard segmentation tool [45]. Watershed methods on the other hand are further advanced and apply a topographic surface which is then virtually filled with water until the virtual valleys are flooded in order to separate objects which would be connected with a threshold approach [46]. Interactive segmentation on the other hand requires additional input supplied by the user. Ahmren et al. [47] argue in their evaluation study on interactive image segmentation that semi-automated approaches turn out to be beneficial for the user for complex segmentation tasks. Fibre tracking is a

Fig. 6. Rendered reconstructed X-ray computer tomography data of the Sample-G with a size of 375 × 925 × 1900 pixels and a voxel size of 10.94 μm displayed in the commercial software package Avizo™. The rendered data reflects a physical size of 4.103 × 10.12 × 20.79 mm³. The full data set can be downloaded at [43].

segmentation method specifically developed for materials composed of long and slender structures [18]. Applications for this approach can vary from human body tissue to fibre reinforced composites.

To decide which segmentation method to use, it is important to define the objective of the analysis already at the beginning of the procedure. It will not be of great value to have high resolution images and a segmentation capturing all details, if the size of the mesh created later on is much too coarse to reflect all this information. This greatly influences the efficiency of the segmentation and meshing. The examined composite layup in the current study is a real challenge for all common segmentation approaches. The fibre bundles are in contact over large areas with almost the same fibre orientation at many places and there are a lot of details visible in the X-ray scan. The original scanned volume was shortened in length from around 20 mm to 10 mm in order to reduce the computation effort for segmentation, meshing and simulation.

Manual segmentation is not desired due to its many disadvantages such as time intensity, non-repeatability and uncertain accuracy. For the investigated composite architecture and the large field of view in this study, manual segmentation would be too time consuming. Consequently, automated methods must be developed. Therefore, three different new methods were developed during this study and compared in Table 6.

The three newly created segmentation approaches are based on the fibre tracking tool available in the commercial software package Avizo™. These methods differ in procedure stemming from the tracked fibres onward. The fibre tracking consists of the two steps "Trace Correlation Lines" and "Cylinder Correlation". The most important parameters "Minimum Seed Correlation: 180, Minimum Continuation: 150, Minimum Distance: 17, Cylinder Length: 100, Outer Cylinder Radius: 12" were chosen based on trails and information published by Karamov et al. [29]. The fibre orientation was filtered with "TensorZZ > 0.95" for unidirectional fibres and "TensorZZ < 0.5 && OrientationPhi < ±190" for ±80° backing fibres. The result of the fibre tracking can be seen in Fig. 7. It must be mentioned that this fibre tracking is computational expensive. For this method a CUDA (Compute Unified Device Architecture) device on the graphics card is necessary. Even with a workstation (CPU 256 Gigabyte and a Nvidia Quadro K6000) especially designed for such tasks, the segmentation can last four to six hours. Similar time periods were reported in another study as well [29]. The tracked fibres were used as input for the *Single Bundle* method. Only the combination of fibre tracking, watershed methods as well as morphological operations allows to obtain single and separate bundle segmentation. In the end still some parts of the bundles required manual separation. This manual segmentation was with a few minutes work more time efficient than further morphological operations in Avizo™. The result can be seen in Fig. 8. Even though this segmentation approach was successful in terms of obtaining separate fibre bundles in an almost fully automated way, there are downsides. The *Single Bundle* method is complex and has a long computation time. Further, several segmentation parameters need to be updated when a new material lay-up is scanned and analysed. Also, the handling of the huge amount of data can be regarded as bottle neck.

The 3D fibre tracking of Avizo™ cannot only serve as basis for the *Single bundle* method but also be used to assign element-wise individual material orientations in the finite element model. This does not
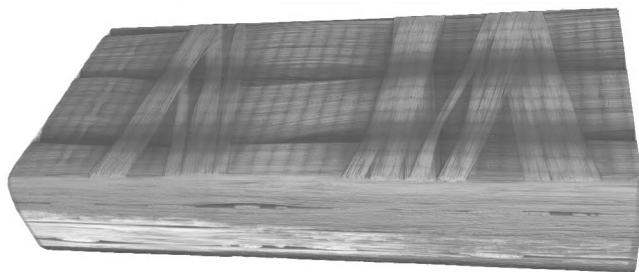
Table 6

Comparison of the three developed segmentation methods regarding accuracy, repeatability, time & software cost and degree of automation. The symbols -, o and + signify disadvantageous, neutral and beneficial properties in the regarded category.

Segmentation method	Accuracy segmentation	Repeatability	Time & software cost	Degree of automation
Single Bundles	o	o	o	-
Physical Boundary	o	o	+	o
Thresholding	+	+	+	+
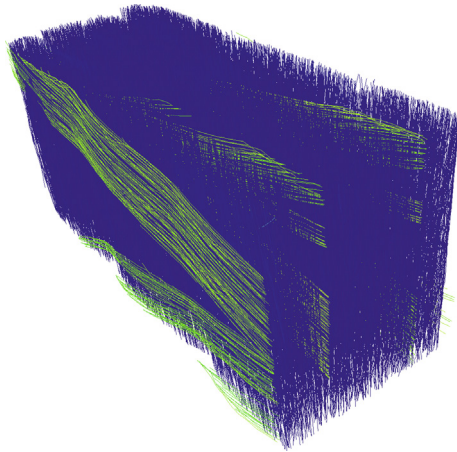
Fig. 7. Tracking of fibres by assigning cylinders with the commercial software package Avizo™.

Fig. 9. Automated segmentation with a physical boundary representation between unidirectional (blue) and backing bundles (green) (left) and thresholded fibre bundles (right) with the commercial software package Avizo™. (For interpretation of the references to color in this figure legend, the reader is referred to the web version of this article.)
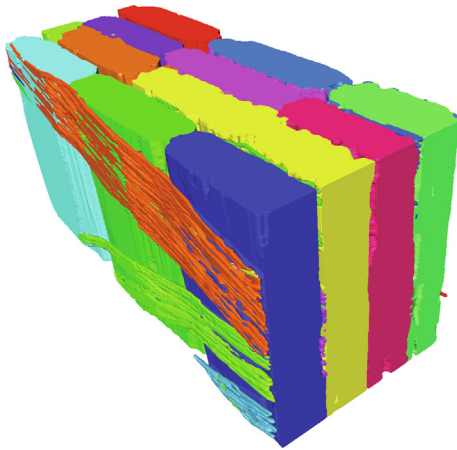

Fig. 8. Single bundles segmented with an almost fully automated method with the commercial software package Avizo™.

only increase the accuracy of the simulation results but also allows faster, simpler and more precise segmentation approaches. Two segmentation approaches are cogitable to take advantage of the fibre orientation. The first method is to use a physical boundary representation between backing and unidirectional bundles, the other one is to regard all fibre bundles as one volume. For the *Physical Boundary* method a combination of 3D fibre tracking, thresholding and morphological operations is necessary. With the second, *Thresholding* method the morphological operations can be spared. Furthermore, the *Thresholding* method is more accurate in terms of bundle material to matrix volume ratio. The results for both segmentation methods can be seen in Fig. 9.

The *Thresholding* method was identified as the fastest and most accurate among the three methods. In addition, it offers a high repeatability and full automation. Consequently, the *Thresholding*
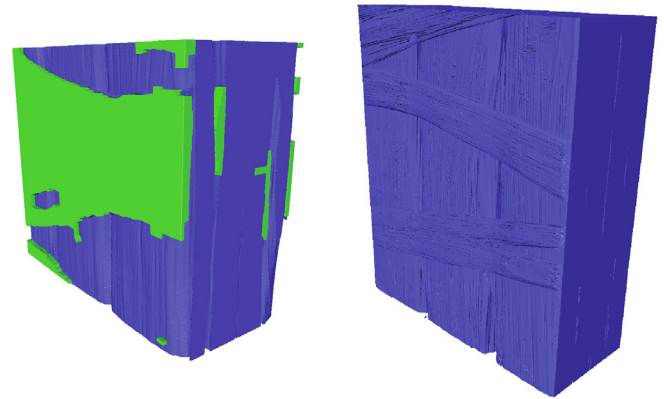
method was elected and is used throughout the remainder of this study.

3.3. Meshing

Finite element modelling always includes a reduction of the physical behaviour. All details and mechanisms cannot be represented in the model. However, the aim for the current study is to capture all relevant mechanisms and effects. That includes influences the stiffness values and possible stress concentration on the fibre bundle scale while keeping the element number as low as possible to allow fast computation. The original surface mesh in Avizo™ has approximately 20 million elements after the segmentation. This amount is reduced to 5 million elements in Avizo™ and exported to the finite element preprocessor ANSA™. Imported in ANSA™, the average mesh size was set to 120 μm compared to fibre diameters of 9, 17 and 24 μm. After depenetration operations and a mesh clean-up, a model with approximately 100,000 surface elements was obtained. This process takes approximately two hours. With the surface mesh ready, a volume mesh was generated. After the bundle meshing, the matrix was created around the bundles. The matrix meshing can become challenging since a negative imprint volume including the bundle surface is necessary. In ANSA™ there is a simple function ("Include solid facets in detection") in the process of the mesh creation that automatically takes care of this issue. In the end the model comprises of approximately 1.5 million tetrahedral elements (Fig. 10).

3.4. Mapping

After the solid mesh generation, the material orientation was mapped. Misaligned fibres reduce the stiffness along the fibre direction drastically. This is due to the difference in the elastic modulus in the longitudinal and transverse directions. For the investigated composite material, the factor is approximately four (see Table 3). Implementing local fibre orientation will therefore improve the quality of the finite
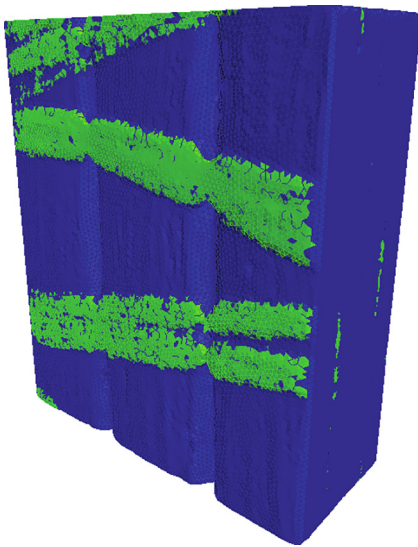
Fig. 10. Figure showing meshed unidirectional bundles in blue and backing bundles in green in ANSA™. The matrix mesh is masked. (For interpretation of the references to color in this figure legend, the reader is referred to the web version of this article.)

element results in contrast to a mean bundle orientation as in [38]. Here the orientation information that was obtained by the 3D fibre tracking in Avizo™ was mapped to all fibre bundle elements. For this purpose the ANSA™ function "Result Mapper" was used. The user must supply a python script that imports the entities from the comma separated values files exported from Avizo™. The ANSA™ mapping tool then searches for each finite element centre for the smallest distance to an orientation information in the files supplied by the
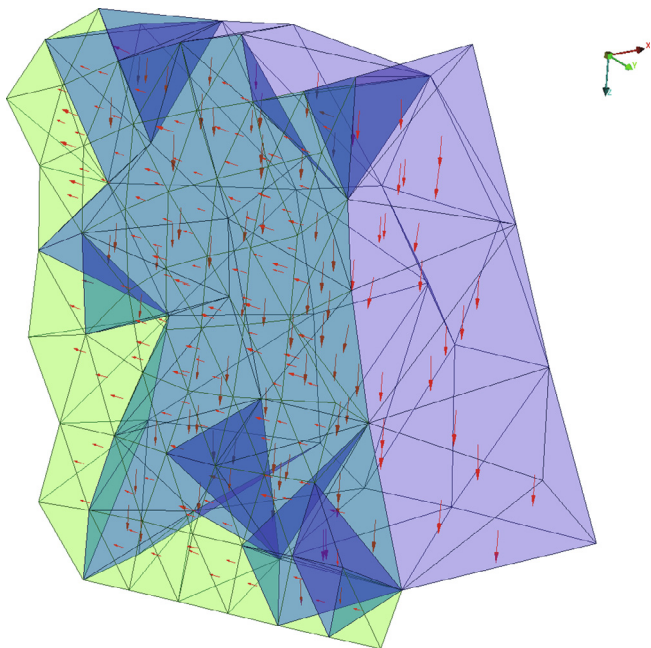

Fig. 11. Material orientation for each single element based on the information of the 3D fibre tracking in Avizo™ mapped in the finite element pre-processor ANSA™ for a small part of the model. Red arrows indicate the element-wise fibre orientation. Elements in blue belong to unidirectional with around 0° and elements in green to backing bundles with ±80°. The finished models can be downloaded at [43]. (For interpretation of the references to color in this figure legend, the reader is referred to the web version of this article.)

user. In addition, elements sets based on the orientation of the elements are generated. This allows different material properties for the unidirectional and backing bundles. The result of fibre mapping and element set definition can be seen in Fig. 11.

Overall can be stated that this method includes local fibre orientation obtained at high resolution. However, it has to be kept in mind that the fibre volume fraction is still determined globally and is the same for all unidirectional bundle elements.

Since bundles and matrix share the same nodes at their common boundary there is no need for contacts. After the model is set-up, a strain of 0.25% along the main fibre direction in an implicit time-integration step in the commercial finite element code ABAQUS™ was applied. The material parameters described in Table 3 were used for the material model. The finished models can be downloaded at [43]. The results are discussed in the following chapter.

4. Results

The X-ray computer tomography scans of Sample-A, Sample-E and Sample-G were modelled and simulated based on the *Thresholding* segmentation method. Table 7 shows a comparison of the normalised stiffness values between the physical tests (Table 4) and the outcome of the X-ray computer tomography aided engineering (XAE) process.

It can be stated that the proposed method allows a precise prediction of the tensile stiffness, underestimating the stiffness by 2.8% on average. Furthermore, the normalised stiffness measured in the physical tests was found to vary between 0.51 and 0.54 (i.e. by 5.6%). In contrast, the predicted normalised stiffness between samples was only 0.2% (ranging between 0.50 and 0.51). The complex process to transfer X-ray computer tomography data to simulation results induces not only errors due the finite element modelling but more importantly due to the image analysis processes. The accuracy of the developed methodology does not suffice to predict the correct trend. However, Sample-E shows the highest stiffness in both physical and virtual test.

The influence of the modelling parameters (Table 8) is investigated in order to assess their error contribution. Firstly the average mesh size was reduced from 120 μm to 50 μm. This increases drastically the number of elements from approximately 1.5 to 12 million. The stiffness results do not change significantly. In addition, beside the increased computational effort (+300%) also longer meshing time and distorted elements resulting in convergence issues must be considered. Secondly, the used 1*st* order tetrahedral elements have the tendency to deliver too high stiffness. This effect is more extensive for bending load cases. For this tensile load case 2*nd* order tetrahedral elements deliver an insignificantly lower stiffness. The increased computational effort (+1000%) is also in this aspect a factor that must be accounted for. In summary it is found that 2*nd* order elements do not offer increased accuracy in predictions, but drastically increase the computational cost.

Since the error contribution of the modelling part is found to be negligible, the reason for deviations between physical and virtual tests must be found in the segmentation process; and here in particular in the mean fibre orientation, the fibre volume fraction and the bundle to volume ratio. The results are listed in Table 9.

Sample-E has the lowest ratio of bundles to the entire volume (determined in the finite element model). In the end Sample-E still deliv-

Table 7

Results of the tensile stiffness comparing the physical tests and the finite element model normalised with the H+ glass fibre stiffness.

	Sample-A	Sample-E	Sample-G
Physical test	0.51	0.54	0.52
XAE result	0.51	0.51	0.50
Difference	+0.3%	-4.8%	-3.2%

Table 8

Influence of modelling on the stiffness results normalised with the H+ glass fibre stiffness comparing the physical test with 1*st* order elements, reduced average mesh size of 50 μm instead of 120 μm and 2*nd* order elements with mesh size 120 μm for Sample-G.

	Physical test	1*st* order elements	reduced element size	2*nd* order elements
Sample-G	0.52	0.50	0.49	0.49

Table 9

Parameters originating form the segmentation influencing the stiffness values determined in the finite element model.

	Sample-A	Sample-E	Sample-G
Normalised fibre bundle stiffness E_{11}	0.61	0.63	0.60
Bundles to full volume ratio	0.88	0.86	0.87
Mean unit vector fibre orientation segmentation	$\begin{pmatrix} 0.00301 \\ 0.00573 \\ 0.99125 \end{pmatrix}$	$\begin{pmatrix} 0.0016 \\ 0.00428 \\ 0.99408 \end{pmatrix}$	$\begin{pmatrix} 0.00195 \\ 0.00796 \\ 0.99008 \end{pmatrix}$
Mean unit vector fibre orientation simulation	$\begin{pmatrix} 0.00129 \\ -0.0073 \\ 0.99997 \end{pmatrix}$	$\begin{pmatrix} 0.00587 \\ -0.0045 \\ 0.99997 \end{pmatrix}$	$\begin{pmatrix} 0.00078 \\ -0.0101 \\ 0.99995 \end{pmatrix}$

ers the highest stiffness value, since it has the highest fibre bundle stiffness in the main fibre direction. The fibre bundle stiffness is purely (except from the constituent properties) depended on the fibre volume fraction inside the fibre bundles. Sample-A and Sample-G on the other hand have nearly the same bundle to volume ratio, but the fibre bundle stiffness is slightly higher for Sample-A. That becomes the decisive factor for a higher simulated stiffness for Sample-A. Those relatively small differences in the parameters fibre bundle stiffness and bundles to full volume ratio are regarded to have a significant influence. A minor influence is observed for the fibre orientation information. The important value for the stiffness results, the third component of the unit vector from the ABAQUS™ input file, is the same for all three samples for the first four significant digits. It can be further seen that the mapping tool works well comparing the results from the segmentation and simulation mean unit vectors, even though the mean unit vectors for the fibre orientations do not match perfectly. The small deviation can be explained with the mapping process where only one of the unit vectors from the all tracked fibre centre lines in Avizo™ is chosen to represent the local material orientation of a single element.

It can be concluded that the segmentation outcome influences significantly the results of the simulated stiffness, in particular the correct bundle volume representation which affects both the calculated fibre bundle stiffness and the bundle to matrix ratio. Consequently, this underlines the high importance of the segmentation method's accuracy. The fibre orientation tracking and mapping do not play a decisive role for this type of composite layup with highly aligned fibres.

Other parameters have no or limited influence on the results. The different image acquisition parameters used for the three scans of Sample-A, Sample-E and Sample-G did not show a detectable influence. The segmentation approach using thresholding and 3D fibre tracking is very robust. However, a proper attenuation contrast between the fibres and matrix must be ensured. It is further found that a resolution of $10.94 \mu m$ is sufficient. Using half the resolution as for the scan of Sample-E neither improves the results nor accelerates the modelling procedure. An investigation to determine the required minimal resolution size for an accurate fibre mapping was not carried out. This would be worth looking into further in the future.

The second goal was to analyse the stress distributions. Slicing through the volume at all positions where the backing bundles are overlapping the unidirectional bundles, stress concentrations inside the unidirectional bundles become visible (Fig. 12). These localised stresses are captured even though an average element size of approximately seven times the fibre diameter was used. Consequently, the

stresses are even higher for the areas closest to the boundary. The precise value of the stress concentrations is difficult to validate. Further research is necessary here. The segmentation algorithm presented in the previous chapter with a physical boundary representation between unidirectional and backing bundles could deliver more information about the actual stress state. However, the results match the experimental observations by Jespersen et al. [5]. They identified stress concentrations at areas of overlapping backing bundles to cause fibre failures inside the unidirectional bundles during tension–tension fatigue loading.

5. Discussion

The key challenge for this study was to create an accurate, fast and repeatable segmentation process. Basis for such a process is a proper attenuation contrast between fibre and matrix. Also the images must not contain major reconstruction artefacts. The segmentation accuracy, and here especially the segmented volumes, has proven to be very important for the finite element results. Huang et al. [31] recently published an approach segmenting individual bundles of woven composites that achieves a high accuracy, but it is a manual method and the issue of repeatability remains [48]. In contrast to their manual approach of segmenting individual fibre bundles, a nearly automated method in Avizo™ is presented in this study. The basis of this approach is fibre tracking. We show that a resolution to fibre diameter of approximately 50% is sufficient to generate accurate predictions with the proposed XAE process. This is in contrast to earlier results by Karamov et al. [29] who stated that resolutions many times smaller than the fibre diameter are needed for accurate fibre tracking in Avizo™. In our presented approach, the focus is on the bundle level rather than on the fibre level. The fibres only serve as basis for the segmentation and provides orientation information for the finite element material modelling. One finite element representing dozens of fibres creates no need for accurate fibre tracking but for an accurate mean fibre orientation. However, in the end, the nearly automated single bundle segmentation was not pursued further due to the complexity of the approach. Using fibre tracking in combination with one of the fastest and most accurate segmentation methods, thresholding, was regarded as more promising. Thresholding also circumvents the risk of penetrations between bundles/fibres itself or with the surrounding matrix and allows an accurate reflection of the fibre bundle to matrix ratio. Using the fibre tracking to assign local fibre orientations can be seen as major advantage of this proposed method compared to the more global material orientation assignment presented in studies from Blinzler et al. [38] and Jespersen et al. [40].

Even though the segmentation method is automated, the user needs experience in Avizo™ to set the right parameters depending on the composite architecture and the fibre to matrix contrast. In addition to the software cost, expensive hardware is also necessary to carry out the 3D fibre tracking in Avizo™. The fibre tracking part of the XAE process is the most time consuming with four to six hours on the reported machine. This time can however be reduced since only limited information is actually used for the element-wise fibre mapping. Further research is needed on how to reduce this time. Besides from tracking, the approach is based on thresholding, which can be done with other software codes such as Matlab® or Python or even freeware like 3D Slicer. The challenge of creating a surface mesh based on the segmented volume, that can be used for a reasonable 3D mesh,
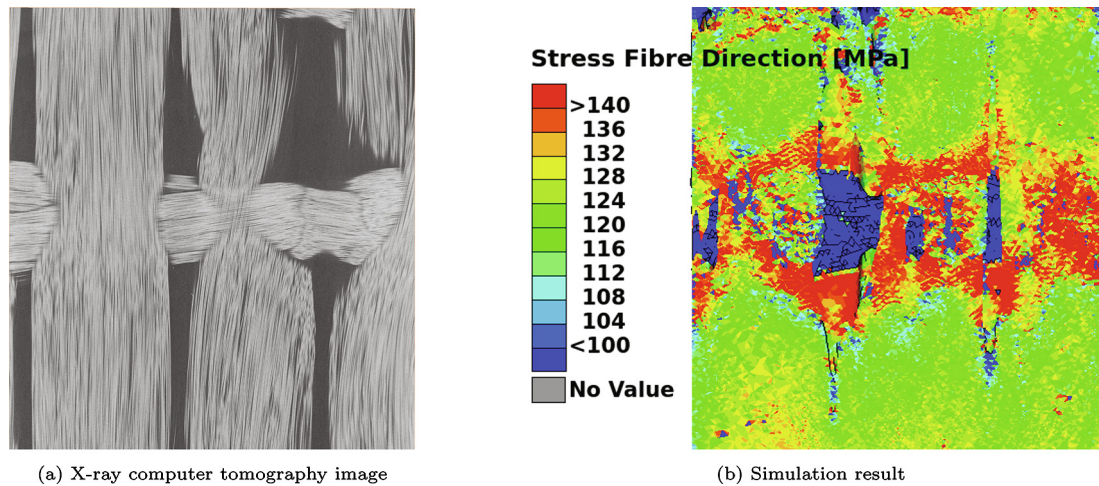
(a) X-ray computer tomography image   (b) Simulation result

Fig. 12. XAE process where X-ray computer tomography data (a) was transferred into finite element model results (b). The plane cuts through the volumes visualise the stress concentrations inside the unidirectional bundles (b) at the position of the overlapping backing bundle (a).

is difficult, even for state-of-the-art finite element pre-processors. An experienced operator needs around two hours for the described volumes. The reason here lies in the complex geometry that comes with the high image resolution required for fibre tracking. Before surface simplification, the volumes had approximately 20 million surface elements. The reduction of the element number to around 100,000 surface elements for a reasonable model with approximately 1.5 million solid elements, most likely, leads to mesh quality issues and penetrations. This makes an entire automated procedure from segmentation to meshing and modelling almost impossible. However, the element-wise fibre orientation mapping is mostly automated. In the end the results can be obtained within eight working hours if the 3D fibre tracking runs over night. The generated finite element analysis results produced by the proposed XAE process are highly accurate. They also show a clear influence of the three parameters originating from the automated segmentation mean fibre orientation, fibre volume fraction and the bundle to volume ratio. The uncertainty induced with the segmentation process is however higher than the differences between the single physical tests. Further improvements are necessary to reduce the segmentation influence on the final finite element results.

6. Conclusion

Non-crimp fabric reinforced composites are extensively used in wind turbine blades since they offer a high tensile stiffness and durability. For improving the stiffness on the large scale, it must be understood how the stiffness on the fibre bundle level influences the global stiffness. Many recent studies have shown how X-ray computer tomography can be used to analyse mechanical properties of glass-fibre reinforced composites. In this study we propose a novel, highly automated X-ray computer tomography aided engineering (XAE) process that transfers X-ray computer tomographic data to accurate and robust finite element model results for non-crimp fabric reinforced composites on the fibre bundle scale. This is the first study that comprises the entire process from image acquisition to modelling using a comparably large volume of approximately $9 \times 4 \times 10$ mm^3 including the orientation information of tens of thousand fibres. The main advantages are the accurate, automated and repeatable segmentation approach and the element-wise fibre mapping. In this study, three tested tensile samples were scanned and analysed with the developed process, with the procedure discussed in Chapter 3. By comparing the simulated and tested stiffness, it can be asserted that the tensile stiffness for the three samples is predicted with an average deviation of 2.8%. The second goal was to analyse the stress distribution inside the fibre bundles.

These results support experimental observations by Jespersen et al. [5] that stress concentrations occur inside the unidirectional bundles in the region where the backing bundles overlap. However, the validation of those stress values requires further research.

The main advantages of our proposed XAE process can be summarised as:

a) Automated approach which allows accurate, fast and repeatable segmentation
b) Includes discrete element-wise local fibre orientation for a more accurate reflection of the mechanical properties of fibre bundles
c) Contains the full procedure including segmentation, fibre tracking, meshing as well as a micro-mechanical model
d) Large fields of views with tens of thousand of fibres

7. Data availability

The raw data required to reproduce these findings are available to download from [43]. The processed data required to reproduce these findings are available to download from [43].

CRediT authorship contribution statement

Robert M. Auenhammer: Methodology, Software, Validation, Formal analysis, Investigation, Writing - original draft, Writing - review & editing, Visualization. **Lars P. Mikkelsen:** Conceptualization, Supervision, Resources, Validation, Writing - review & editing, Funding acquisition. **Leif E. Asp:** Funding acquisition, Supervision, Writing - review & editing, Validation. **Brina J. Blinzler:** Validation, Writing - review & editing, Funding acquisition.

Declaration of Competing Interest

The authors declare that they have no known competing financial interests or personal relationships that could have appeared to influence the work reported in this paper.

Acknowledgements

References

[1] Agarwal B, Broutman L, Chandrashekhara K. Analysis and performance of fiber composites. 4th ed. Hoboken/NJ, USA: Wiley; 2018.

[2] Liotier PJ, Alain V, Christine D. Characterization of 3D morphology and microcracks in composites reinforced by multi-axial multi-ply stitched preforms. Compos Part A Appl Sci Manuf 2010;41(5):653–62. https://doi.org/10.1016/j.compositesa.2010.01.015.

[3] Mikkelsen LP, Emerson MJ, Jespersen KM, Dahl VA, Conradsen K, Dahl AB. X-ray based micromechanical finite element modeling of composite materials. In: 29th Nordic seminar on computational mechanics Gothenburg, Sweden.

[4] Mikkelsen LP. The fatigue damage evolution in the load-carrying composite laminates of wind turbine blades. In: Fatigue life prediction of composites and composite structures. Duxford, United Kingdom: Elsevier Ltd.; 2020. https://doi.org/10.1016/b978-0-08-102575-8.00016-4.

[5] Jespersen KM, Glud JA, Zangenberg J, Hosoi A, Kawada H, Mikkelsen LP. Uncovering the fatigue damage initiation and progression in uni-directional non-crimp fabric reinforced polyester composite. Compos Part A Appl Sci Manuf 2018;109:481–97. https://doi.org/10.1016/j.compositesa.2018.03.002.

[6] Ostachowicz W, McGugan M, Schröder-Hinrichs JU, Luczak M. MARE-WINT: New materials and reliability in offshore wind turbine technology. Springer Open 2016. https://doi.org/10.1007/978-3-319-39095-6.

[7] Aquill A, Bond L. Computed tomography reconstruction techniques. In ASM Handbook, Nondestructive Evaluation of Materials (2018 Revision), vol. 17. Ohio, USA: ASM International; 2018. URL:https://app.knovel.com/hotlink/toc/id: kpASMHVN06/asm-handbook-volume-17/asm-handbook-volume-17..

[8] Clack R. Towards a complete description of three-dimensional filtered backprojection. Phys Med Biol 1992;37(3):645–60. https://doi.org/10.1088/0031-9155/37/3/011.

[9] Batenburg KJ, Plantagie L. Fast approximation of algebraic reconstruction methods for tomography. IEEE Trans Image Process 2012;21(8):3648–58. https://doi.org/10.1109/TIP.2012.2197012.

[10] H. Der Sarkissian, F. Lucka, M. van Eijnatten, G. Colacicco, S.B. Coban, K.J. Batenburg. A cone-beam X-ray computed tomography data collection designed for machine learning. Sci Data 2019;6(1):215. arXiv:1905.04787. https://doi.org/10.1038/s41597-019-0235-y.

[11] Zhuge X, Jinnai H, Dunin-Borkowski RE, Migunov V, Bals S, Cool P, Bons AJ, Batenburg KJ. Automated discrete electron tomography – towards routine high-fidelity reconstruction of nanomaterials. Ultramicroscopy 2017;175:87–96. https://doi.org/10.1016/j.ultramic.2017.01.009.

[12] Buurlage JW, Kohr H, Palenstijn JW, Batenburg JK. Real-time quasi-3D tomographic reconstruction. Meas Sci Technol 2018;29(6):. https://doi.org/10.1088/1361-6501/aab754064005.

[13] Harimon MA, Miyashita Y, Otsuka Y, Mutoh Y, Yamamoto S. High temperature fatigue characteristics of P/M and hot-forged W-Re and TZM for X-ray target of CT scanner. Mater Des 2018;137:335–44. https://doi.org/10.1016/j.matdes.2017.10.044.

[14] Ren W, Yang Z, Sharma R, Zhang C, Withers PJ. Two-dimensional X-ray CT image based meso-scale fracture modelling of concrete. Eng Fract Mech 2015;133:24–39. https://doi.org/10.1016/j.engfracmech.2014.10.016.

[15] Naeimi M, Li Z, Qian Z, Zhou Y, Wu J, Petrov RH, Sietsma J, Dollevoet R. Reconstruction of the rolling contact fatigue cracks in rails using X-ray computed tomography. NDT E Int 2017;92:199–212. https://doi.org/10.1016/j.ndteint.2017.09.004.

[16] Wang Y, Mikkelsen LP, Pyka G, Withers PJ. Time-lapse helical X-ray computed tomography (CT) study of tensile fatigue damage formation in composites for wind turbine blades. Materials 2018;11:2340. https://doi.org/10.3390/ma11112340.

[17] Garcea S, Wang Y, Withers P. X-ray computed tomography of polymer composites. Compos Sci Technol 2018;156:305–19. https://doi.org/10.1016/J.COMPSCITECH.2017.10.023.

[18] Emerson MJ, Dahl VA, Conradsen K, Mikkelsen LP, Dahl AB. Statistical validation of individual fibre segmentation from tomograms and microscopy. Compos Sci Technol 2018;160:208–15. https://doi.org/10.1016/j.compscitech.2018.03.027.

[19] Favata J, Shahbazmohamadi S. Realistic non-destructive testing of integrated circuit bond wiring using 3-D X-ray tomography, reverse engineering, and finite element analysis. Microelectr Reliab 2018;83:91–100. https://doi.org/10.1016/j.microrel.2018.02.015.

[20] Wang Y, Chai Y, Soutis C, Withers PJ. Evolution of kink bands in a notched unidirectional carbon fibre-epoxy composite under four-point bending. Compos

[21] Sci Technol 2019;172:143–452. https://doi.org/10.1016/j.compscitech.2019.01.014.

[21] Wilhelmsson D, Mikkelsen LP, Fæster S, Asp LE. Influence of in-plane shear on kink-plane orientation in a unidirectional fibre composite. Compos Part A Appl Sci Manuf 2019;119:283–90. https://doi.org/10.1016/j.compositesa.2019.01.018.

[22] Zangenberg J, Brøndsted P, Gillespie JW. Fatigue damage propagation in unidirectional glass fibre reinforced composites made of a non-crimp fabric. J Compos Mater 2014;48(22):2711–27. https://doi.org/10.1177/0021998313502062.

[23] Kim J, Kagias M, Marone F, Stampanoni M. X-ray scattering tensor tomography with circular gratings. Appl Phys Lett 2020;116:. https://doi.org/10.1063/1.5145361134102.

[24] Mirkhalaf SM, Eggels E, Anantharanga AT, Larsson F, Fagerström M. Short fiber composites: computational homogenization vs orientation averaging. In: Proceedings of the 22nd international conference on composite materials Melbourne, Australia.

[25] Kammoun S, Doghri I, Adam L, Robert G, Delannay L. First pseudo-grain failure model for inelastic composites with misaligned short fibers. Compos Part A Appl Sci Manuf 2011;42(12):1892–902. https://doi.org/10.1016/j.compositesa.2011.08.013.

[26] Kagias M, Wang Z, Birkbak ME, Lauridsen E, Abis M, Lovric G, Jefimovs K, Stampanoni M. Diffractive small angle X-ray scattering imaging for anisotropic structures. Nat Commun 2019;10:5130. https://doi.org/10.1038/s41467-019-12635-2.

[27] Advani SG, Tucker CL. The use of tensors to describe and predict fiber orientation in short fiber composites. J Rheol 1987;31(8):751–84. https://doi.org/10.1122/1.549945.

[28] Bay RS, Tucker CL. Fiber orientation in simple injection moldings. Part I: Theory and numerical methods. Polym Compos 1992;13(4):317–31. https://doi.org/10.1002/pc.750130409.

[29] Karamov R, Martulli LM, Kerschbaum M, Sergeichev I, Swolfs Y, Lomov SV. Micro-CT based structure tensor analysis of fibre orientation in random fibre composites versus high-fidelity fibre identification methods. Compos Struct 2020;235:. https://doi.org/10.1016/j.compstruct.2019.111818111818.

[30] User's guide avizo software; 2019, URL:https://assets.thermofisher.com/TFS-Assets/MSD/Product-Guides/users-guide-avizo-software-2019.pdf [accessed: 2020-02-25]..

[31] Huang W, Causse P, Brailovski V, Hu H, Trochu F. Reconstruction of mesostructural material twin models of engineering textiles based on micro-CT aided geometric modeling. Compos Part A Appl Sci Manuf 2019;124:105. https://doi.org/10.1016/j.compositesa.2019.105481.

[32] Sencu RM, Yang Z, Wang YC, Withers PJ, Rau C, Parson A, Soutis C. Generation of micro-scale finite element models from synchrotron X-ray CT images for multidirectional carbon fibre reinforced composites. Compos Part A Appl Sci Manuf 2016;91(1):85–95. https://doi.org/10.1016/j.compositesa.2016.09.010.

[33] Li Y, Sun B, Gu B. Impact shear damage characterizations of 3D braided composite with X-ray micro-computed tomography and numerical methodologies. Compos Struct 2017;176:43–54. https://doi.org/10.1016/J.COMPSTRUCT.2017.04.067.

[34] Straumit I, Lomov SV, Wevers M. Quantification of the internal structure and automatic generation of voxel models of textile composites from X-ray computed tomography data. Compos Part A Appl Sci Manuf 2015;69:150–8. https://doi.org/10.1016/J.COMPOSITESA.2014.11.016.

[35] Badel P, Vidal-Sallé E, Maire E, Boisse P. Simulation and tomography analysis of textile composite reinforcement deformation at the mesoscopic scale. Compos Sci Technol 2008;68(12):2433–40. https://doi.org/10.1016/j.compscitech.2008.04.038.

[36] Naouar N, Vidal-Salle E, Schneider J, Maire E, Boisse P. 3D composite reinforcement meso F.E. analyses based on X-ray computed tomography. Compos Struct 2015;132:1094–104. https://doi.org/10.1016/j.compstruct.2015.07.005.

[37] Iizuka K, Ueda M, Takahashi T, Yoshimura A, Nakayama M. Development of a three-dimensional finite element model for a unidirectional carbon fiber reinforced plastic based on X-ray computed tomography images and the numerical simulation on compression. Adv Compos Mater 2019;28(1):73–85. https://doi.org/10.1080/09243046.2018.1434731.

[38] Blinzler BJ, Wilhelmsson D, Asp LE, Jespersen KM, Mikkelsen LP. A systematic approach to transforming composite 3D images into meso-scale computational models. In: 18th European conference on composite materials, Athens, Greece.

[39] Tao W, Zhu P, Xu C, Liu Z. Uncertainty quantification of mechanical properties for three-dimensional orthogonal woven composites. Part II: Multiscale simulation. Compos Struct 2020;235:. https://doi.org/10.1016/j.compstruct.2019.111764111764.

[40] Jespersen KM, Asp LE, Hosoi A, Kawada H, Mikkelsen LP. X-ray tomography based finite element modelling of non-crimp fabric based fibre composite. In: 18th European conference on composite materials, Athens, Greece.

[41] Jespersen KM, Zangenberg J, Lowe T, Withers PJ, Mikkelsen LP. Fatigue damage assessment of uni-directional non-crimp fabric reinforced polyester composite using X-ray computed tomography. Compos Sci Technol 2016;136:94–103. https://doi.org/10.1016/j.compscitech.2016.10.006.

[42] Omairey SL, Dunning PD, Sriramula S. Development of an ABAQUS plugin tool for periodic RVE homogenisation. Eng Comput 2019;35(2):567–77. https://doi.org/10.1007/s00366-018-0616-4.

[43] R.M. Auenhammer, L.P. Mikkelsen, L.E. Asp, B.J. Blinzler. Automated x-ray computer tomography segmentation method for finite element analysis of non-crimp fabric reinforced composites [Data set]. Zenodo. URL: http://doi.org/10.5281/zenodo.3830790.

[44] Van Leeuwen T, Maretzke S, Batenburg KJ. Automatic alignment for three-dimensional tomographic reconstruction. Inverse Prob 2018;34:. arXiv:arXiv:1705.08678v4, doi:10.1088/1361-6420/aaa0f8024004.

[45] Maire E, Withers PJ. Quantitative X-ray tomography. Int Mater Rev 2014;59(1):1–43. https://doi.org/10.1179/1743280413Y.0000000023.

[46] Gaetano R, Masi G, Poggi G, Verdoliva L, Scarpa G. Marker-controlled watershed-based segmentation of multiresolution remote sensing images. IEEE Trans Geosci Remote Sens 2015;53(6):2987–3004. https://doi.org/10.1109/TGRS.2014.2367129.

[47] Amrehn M, Steidl S, Kortekaas R, Strumia M, Weingarten M, Kowarschik M, et al. A semi-automated usability evaluation framework for interactive image segmentation systems. Int J Biomed Imag 2019:1–21. https://doi.org/10.1155/2019/1464592.

[48] Sinchuk Y, Kibleur P, Aelterman J, Boone MN, Paepegem WV. Variational and deep learning segmentation of very-low-contrast X-ray computed tomography images of carbon/epoxy woven composites. Materials 2020;13(4):936. https://doi.org/10.3390/ma13040936.